



Optical and electrical design guidelines for ZnO/CdS nanorod-based CdTe solar cells

CAN OZCAN,^{1,2} DENIZ TURKAY,^{1,3} AND SELCUK YERCI^{1,2,3,*}

¹Center for Solar Energy Research and Applications (GUNAM), Middle East Technical University, Ankara, Turkey

²Electrical and Electronics Engineering Department, Middle East Technical University, Ankara, Turkey

³Department of Micro and Nanotechnology, Middle East Technical University, Ankara, Turkey

*syerci@metu.edu.tr

Abstract: An alternative structure to planar CdTe solar cells is realized by coating ZnO/CdS nanorods (NRs) with a CdTe layer. These structures are expected to achieve high-powered conversion efficiencies through enhanced light absorption and charge carrier collection. ZnO NR-based CdTe solar cell efficiencies; however, they have remained well below their planar counterparts, thus hindering NRs in CdTe solar cells' advantages. Here, we analyze the light trapping and carrier collection efficiencies in two types of ZnO NR-based CdTe solar cells through optical and electrical simulations. The buried CdTe solar cells are formed by completely filling the gaps in between ZnO/CdS NRs. This produces a maximum achievable photo-current of 27.4 mA/cm² when 2000 nm-tall and 20°-angularly-deviated NRs are used. A short-circuit current density of 27.3 mA/cm² is achievable with the same geometry for 5 rods/μm²-dense NRs when a moderate CdTe doping density and a CdS/CdTe surface velocity of 10¹⁶ cm⁻³ and 10⁴ cm/s are used, respectively. We reveal the potential of buried CdTe solar cell for high-charge carrier collection and provide a design guideline in order to achieve high short-circuit current densities with ZnO NR-based CdTe solar cells.

© 2019 Optical Society of America under the terms of the [OSA Open Access Publishing Agreement](#)

1. Introduction

CdTe is a direct bandgap semiconductor with a near optimum bandgap of ~1.5 eV and has a high absorption coefficient near the band edge ($>10^4$ cm⁻¹) making it an excellent material for photovoltaics (PV) [1]. To date, 22.1% and 18.6% efficiencies have been achieved for solar cells and modules, respectively [2]. These properties of CdTe have made it attractive for large-scale solar energy production. In 2017, CdTe solar cells constituted more than 50% of the total global PV production among thin film solar cells having a 2.3% share in the overall PV market [3]. The CdTe solar cells currently available in the PV market are planar superstrate type solar cells. On the contrary, coating an extremely thin absorber (ETA) CdTe layer conformally around randomly-oriented ZnO nanorods (NRs) has been considered as an alternative to the conventional CdTe planar solar cell structure in recent years [4–10]. The efficient light trapping due to enhanced light scattering of ZnO NRs [11,12] and the radial charge carrier collection in ETA CdTe solar cells provide efficient charge carrier generation and collection, respectively [13]. Therefore, one can reduce the CdTe amount in the cell required to achieve high short circuit current densities (J_{sc}). Despite the aforementioned advantages, the reported efficiencies of the solar cells with ZnO/CdTe NR core-shell arrays are lower than 1% [4–6]. Some studies indicated that insertion of a thin CdS interfacial layer between ZnO NRs and CdTe layer increased the efficiencies of CdTe solar cells due to the graded band alignment and reduced defect density at the interfaces [7,8]. Despite the insertion of the CdS interfacial layer, the NR-based CdTe solar cells still performed well-below their planar counterparts [7–10]. The relatively poor performance of NR-based CdTe solar cells can be better understood and strategies to overcome the low performance can be developed by means of optical and electrical simulations.

Among two notable simulation studies in the literature, Michallon et al. [14] reported that the vertical ZnO/CdTe NR structures in the substrate device configuration enhance the maximum achievable photocurrent (MAPC) up to a factor of 1.79 compared to their planar counterparts having the same amount of CdTe. They demonstrated that MAPC values as high as 28 mA/cm² can be achieved when vertical ZnO NR scaffold is used. In another study, Kapadia et al. [15] investigated the J_{sc} , open circuit voltages (V_{oc}) and efficiencies of CdTe solar cells with respect to hole diffusion distance, CdS/CdTe recombination velocity, and CdS nanopillar radius and period for vertical CdS/CdTe nanopillar arrays. Over 22% efficiency and a J_{sc} of 28 mA/cm² were calculated for a relatively high CdTe acceptor doping density of 10¹⁷ cm⁻³. It should be noted that high doping densities are very demanding to achieve because of the self-compensating effect of As dopants in CdTe due to the formation of AX centers and defect formation with a Cd site or Cd vacancy [16]. While a doping density of 10¹⁶ cm⁻³ is achievable for CdTe solar cells, CdTe doping densities as high as 10¹⁷ cm⁻³ would require superior control to the employed dopant amount [17] or utilizing a single crystalline CdTe [18] which is not practical for large scale energy production. It should also be noted that the majority of experimental studies reported in the literature exhibit ZnO NRs having different degrees of random orientation. To authors' knowledge, no optical and electrical analysis on ZnO NR-based CdTe solar cells have been carried out based on experimentally achieved cell geometries and material properties taking into account the parameters such as random orientations of ZnO NRs, relatively low CdTe acceptor doping concentrations and high surface recombination velocities at the CdS/CdTe interface.

In this work, superstrate type ZnO/CdS/CdTe core-shell NR arrays sandwiched between Au and ITO/glass were optically and electrically simulated to obtain absorption spectra and J_{sc} values for various geometrical configurations (i.e. height, density and angular deviation from the vertical) of NRs, CdTe acceptor doping densities and CdS/CdTe surface recombination velocities. The structural parameters and material properties in the simulations were chosen with consideration of the practical limitations. We demonstrate the high absorption capabilities of NR-based solar cells with angularly deviated, tall, and dense ZnO NRs through optical simulations by taking into account the CdTe amount in the solar cells. We identified the factors that determine absorption mechanisms in these structures and quantified the parasitic losses in various layers. The optical results were used as inputs to the electrical simulations to obtain the charge carrier collection efficiency and J_{sc} . The electrical simulation results were used to identify the required NR geometry, CdTe doping densities and CdS/CdTe interface quality for ZnO NR-based CdTe solar cells to outperform their planar counterparts. Our optical and electrical simulation results reveal the loss mechanisms of ZnO NR-based CdTe solar cells. We propose a guideline on the selection of geometrical and material parameters to maximize J_{sc} .

2. Structural design and simulation methodology

ZnO is typically used as a buffer layer in CdTe solar cells, which has a bandgap of 3.2 eV. Therefore, it induces a parasitic absorption of light at wavelengths shorter than 390 nm. ZnO NRs are usually grown by hydrothermal growth [7–9,19], electrochemical growth [10] and chemical bath deposition [20] on a transparent conductive oxide, glass or ZnO seed layer. ZnO NRs have been fabricated as tall as 7 μm [5] and the diameter has ranged between 40 nm and 200 nm [19] depending on the process parameters. Moreover, ZnO NRs densities between ~5 rods/μm² [8] and 60 rods/μm² [9] have been reported in the literature. CdS is an *n*-type material and performs as the window layer in CdTe solar cells. Its band gap of 2.4 eV constitutes a source for absorption at wavelengths shorter than 520 nm, most of which is parasitic. CdTe forms the *p*-type side of the heterojunction and has a bandgap of ~1.5 eV. The high absorption coefficient of CdTe up to its band edge (~850 nm) makes it the dominant absorber for wavelengths between 400 nm and 850 nm. At shorter wavelengths, parasitic losses in ZnO and CdS layers dominate the absorption in the ZnO/CdS NR-based CdTe solar

cells, as will be evident later. Various methods for conformal deposition of CdS and CdTe were reported in the literature such as successive ionic layer adsorption and reaction (SILAR) [7], electrochemical deposition [5,8], metalorganic chemical vapor deposition (MOCVD) [9]. Long deposition times or cycles of CdTe leads to filling of the space in between ZnO/CdS NRs resulting in a buried CdTe layer. In a recent study, we have demonstrated that a cell efficiency of 4.5% can be achieved by buried CdTe layer fabricated by MOCVD [9].

The scanning electron microscope images of the ZnO NRs presented in the aforementioned studies were used to extract the heights, densities, angular deviation from the vertical axis and diameters utilized in this study. The randomly-oriented ZnO NRs were built in the simulation domain on a 30 nm-thick ZnO seed layer and 150 nm-thick ITO layer with heights of 500, 1000 and 2000 nm, diameter of 80 nm and densities of 5, 20 and 50 rods/ μm^2 . We avoided selecting taller and denser NRs than 2 μm and 50 rods/ μm^2 since too tall and dense NRs increase the surface recombination and decrease the charge collection efficiency, as will be evident in the following sections. A 15 nm-thick CdS was assumed to be grown conformally around ZnO NRs. The ZnO/CdS NR core-shell arrays on the ITO/glass superstrate, shown in Fig. 1(a), were coated with a 40 nm-thick CdTe absorber to construct ETA structures. The resultant ZnO/CdS/CdTe NRs were partially filled with a transparent polymer polymethyl methacrylate (PMMA) and filling was completed with Au layer as the back contact as shown in Fig. 1(b) to form ETA type solar cells, referred to as ‘ETA cells’ from now on in this paper. The ratio of PMMA/Au filling was chosen such that at least 90% of the NR tips are in contact with the Au layer. Alternatively, we investigated a structure in which ZnO/CdS NRs are buried in CdTe. The resultant structure will be referred to as the buried structure. The ‘buried cells’, shown in Fig. 1(c), were formed by completely filling the gaps in between ZnO/CdS NRs with CdTe layer with an excess layer of 100 nm on the tips of vertical NRs corresponding to an overgrowth during CdTe deposition [9]. Then, a 150 nm-thick Au back contact was placed on top of the CdTe layer. The ITO layer is assumed to serve as the front contact in both ETA and buried solar cells.

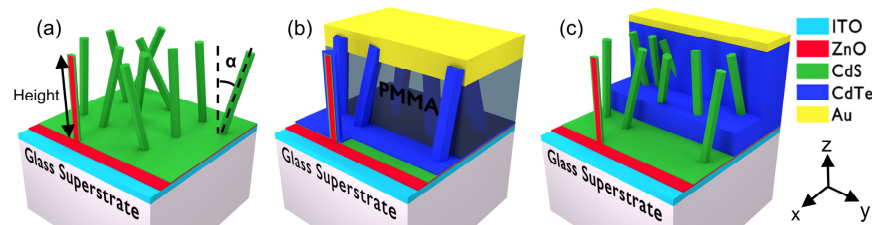


Fig. 1. Schematics of (a) ZnO/CdS NRs prior to CdTe coating, (b) the ETA cell and (c) the buried cell.

The optical simulations of CdTe solar cells was performed using a commercial-grade simulator based on the finite-difference time-domain (FDTD) method [21]. The bases of every individual hexagonally shaped ZnO NRs having desired densities and heights were placed at random locations allowing a minimum distance between NRs changing from 90 nm for the densest NRs to 380 nm for the least dense NRs. Angular deviation from the z-axis of each NR, denoted by α in Fig. 1(a), was also individually and randomly assigned in x- and y-directions assuming a Gaussian distribution with a constant mean of θ and the standard deviations were swept from θ to 2θ . The standard deviation of the Gaussian distribution is referred to as the angular deviation in the rest of this paper and should not be confused with the mean angle of the Gaussian, which is constant and θ .

The sizes of the simulation domain both in x- and y-directions were set to 2000 nm to successfully model the large-scale light scattering effects of ZnO NRs due to their random orientations. The size of the simulation domain in z-direction was changed according to the height of the NRs. Periodic boundary conditions were used at x- and y-boundaries. Perfectly matched layers were used in the wave propagation direction (z-direction). A uniform cubic

mesh with 5 nm was used. A plane wave source with a broad spectral range of 300-900 nm was normally incident on the cell structure from the glass, ignoring the reflection at the air-glass interface. The wavelength spacing was set to 5 nm to obtain highly-resolved absorbance, reflectance and haze spectra. The absorption calculation in each layer of the structures was done by taking 2-D slices from the 3-D structures and averaging the obtained absorption in the 2-D slices, since calculation of the absorption in the whole 3-D simulation domain would require an excessive amount of memory and processing power. Averaging 10 of the 2-D slices were observed to be enough to obtain the absorption in each layer accurately, as above this value the results change only marginally. The photo-generation profiles were calculated by integrating the multiplication of solar photon flux and absorption in each mesh point in the simulation domain for wavelengths shorter than the band edge of CdTe (i.e. 850 nm). The volumetric amount of CdTe layers for each geometry were also calculated from the slices taken from the 3-D structure. The material refractive indices were taken from the literature for ITO [22], ZnO [23], CdS [24], CdTe [24], Au [25] and PMMA [26].

Optical simulations were performed in two steps. First, ZnO/CdS NRs on ITO/glass without the CdTe and Au contact were simulated for the 27 geometrical configurations (3 heights, 3 densities and 3 angular deviations), and the absorption, transmittance and haze spectra were extracted. Second, the ETA and buried cells were simulated, and the absorption, reflection and photo-generation profiles were extracted. The MAPC, used as a figure-of-merit for the optical performance of solar cells, were calculated by the following formula

$$MAPC = \frac{q}{hc} \int_{300nm}^{850nm} \lambda A_{CdTe}(\lambda) \phi_i(\lambda) d\lambda \quad (1)$$

where q is the elementary charge, λ is the wavelength of the incident light, h is the Planck's constant, c is the speed of light in vacuum, A_{CdTe} is the absorption in CdTe layer and ϕ_i is the AM 1.5G solar spectral irradiance. Although photo-generated charge carriers in the CdS layer can be collected, most of the photo-generated charge collection takes place in CdTe layer. We calculated that only ~15% (depending on geometry) of the absorption in CdS contributes to J_{sc} (data not shown); therefore, we neglected CdS absorption when calculating MAPC. This omission does not change the trends in MAPC discussed in the paper. For electrical simulations, the photo-generation in CdS layer is taken into account.

The trends in MAPC for both buried and ETA cells are elucidated by exploring the haze of ZnO/CdS NRs, the CdTe amount in the cells and the parasitic absorption in the ITO, ZnO, CdS and Au layers. Haze is a wavelength dependent performance parameter of light scattering and, in this study, it refers to the scattered portion of the incident light after being transmitted through the ITO layer and ZnO/CdS NRs, subsequently. A hazier NR geometry, in general, favors enhanced light trapping. Nonetheless, the haze must be examined in caution since it is not directly correlated with the absorption in the CdTe layer as the parasitic absorption in CdS is also enhanced with the haze. In conjunction with the haze, the MAPC of both ETA and buried cells are sensitive to the amount of CdTe in the cell structure. The amount of CdTe in a given solar cell structure is expressed as the equivalent thickness which refers to the CdTe layer thickness of a planar solar cell having the same amount of CdTe with a NR-based cell.

The simulations of carrier collection efficiency and J_{sc} for both ETA and buried cells were carried out by Silvaco ATLAS [27]. The effects of the following parameters on J_{sc} were analyzed for both ETA and buried cells: (1) geometrical dimensions of the ZnO NRs (NR height and density), (2) CdTe acceptor concentration (N_A) in the CdTe base, and (3) the surface recombination velocity (S_F) at the CdS/CdTe interface. We considered 2D and periodic NRs with no angular deviation to simplify the calculations and the meshing procedure in electrical simulations. The periods of the NRs were taken equal to the average

distance between the randomly-oriented NRs generated for the optical simulations. The photo-generation profiles of the cells with periodic NRs were obtained through optical simulations. The MAPC values were calculated for each layer in the cells with both periodic and randomly-oriented NRs. Then, the photo-generation rates obtained for the cells with periodic NRs were uniformly scaled for each layer individually to match the MAPC of the cells with randomly-oriented NRs. The scaling was necessary since it was not possible to use the simulated photo-generation profiles of the cells with randomly-oriented NRs directly in the electrical simulations of the cells with periodic NRs simulations. The scaling helps to include the effect of randomly-oriented NRs in the periodic simulations. The scaled photo-generation profiles of the cells with periodic NRs were supplied to electrical simulations as inputs.

The effective density of states, carrier mobility, bandgap values for ITO, ZnO and CdS layers utilized in the electrical simulations were taken from Refs [28–32]. The Shockley-Read-Hall recombination lifetimes of electrons and holes in the CdTe absorber layer were kept constant at 10 ns [15]. To our knowledge, there is no universally observed direct correlation between the doping concentration in CdTe films and SRH lifetimes of minority carriers and carrier mobilities in these films. Therefore, we set these parameters to be constant and independent of doping concentration in CdTe. The dopant concentrations in the ITO, ZnO and CdS layers were kept constant at 10^{20} cm^{-3} , 10^{18} cm^{-3} , and 10^{17} cm^{-3} , respectively [29].

3. Results

3.1 Optical simulations

The buried cells produce higher MAPC than the ETA cells regardless of the ZnO NR geometry as shown in Fig. 2. MAPC increases monotonically with the NR height for a constant NR density and an angular deviation for both ETA and buried cells as shown in Fig. 2. Similarly, the haze of ZnO/CdS NRs and equivalent CdTe thickness also increase with the NR height as shown in Fig. 3(a) and the inset of Fig. 3(a), respectively. Therefore, we conclude that the combination of increasing haze and equivalent thickness helps to enhance the absorption in CdTe despite the increasing parasitic absorption in CdS that appears at short wavelengths and results in a slight red-shift in the haze peak wavelength as shown in Fig. 3(a). Additionally, the parasitic absorption in Au decreases with NR height for the ETA cells since the light intensity reaching the Au rear contact drops simultaneously. It should also be noted that the parasitic absorption in the planar Au contact for the buried cells is much smaller compared to the rough Au contact of the ETA cells.

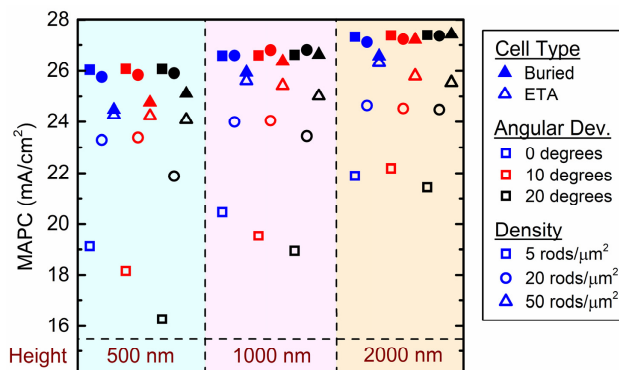


Fig. 2. The MAPC of ETA and buried cells for various heights, angular deviations and densities of ZnO NRs.

The angular deviation boosts haze without significantly increasing the parasitic absorption in CdS as shown in Fig. 3(b). For example, the peak value of haze increases from 0.05 to 0.20 at 530 nm when NRs undergo an angular deviation of 20° . The equivalent thicknesses of ETA and buried cells are independent of the angular deviation since the total surface area and the total occupied space of ZnO/CdS NRs do not change with the angular deviation. As a result, the MAPC of buried cells increase with angular deviation, notably for dense NRs, without further material cost thanks to the enhanced light trapping. On the contrary, the trends of MAPC for ETA cells are ambiguous due to the generally increasing Au parasitic absorption at high angular deviations, which lowers the absorption in CdTe layer. Exemplary Au parasitic absorption spectra are given in the inset of Fig. 3(b) for ETA cells with 1000 nm-tall and 50 rods/ μm^2 -dense NRs for varying angular deviations. ETA cells have high Au parasitic absorption at long wavelengths, which increases further with the angular deviation, mainly due to the increasing Au filling ratio for highly angularly-deviated NRs. Hence, ETA solar cells do not effectively benefit from the enhanced light trapping effects of angularly-deviated NRs.

The haze of ZnO/CdS NRs and parasitic absorption in CdS increase with the NR density as shown in Fig. 3(c). On the other hand, the equivalent thickness shows opposite trends for ETA and buried cells with the NR density as shown in the inset of Fig. 3(c). While denser NRs allow larger CdS surface area for CdTe to grow in the ETA cells, they lead ZnO/CdS NRs to occupy more space and leave less space for CdTe in the buried cells. Despite the increase in the parasitic absorption in CdS, the increasing equivalent CdTe thickness and haze with NR density boost MAPC of ETA cells. The Au parasitic absorption is typically lower for higher NR densities since more light is absorbed in CdTe leaving less light to be absorbed in the Au layer (data not shown). In case of the buried cells, there is a trade-off between the haze and the equivalent CdTe thickness. While increasing haze with NR density helps to achieve a higher MAPC, the reduced equivalent CdTe thickness deteriorates it. MAPC typically decreases with the NR density since the haze cannot compensate for the losses due to the equivalent CdTe thickness reduction and enhanced CdS parasitic absorption. However, MAPC is enhanced with the NR density for cells with 1000 and 2000 nm-tall NRs and the angular deviation of 20° despite the reduced equivalent CdTe thickness due to hazier NR geometries.

It is essential to note that the CdS absorption spectra provided in Figs. 3(a)-3(c) reduce drastically after depositing the absorbing CdTe layer due to a better refractive index matching between CdS and CdTe compared to CdS and air. Nonetheless, the parasitic absorption in CdS still follows the aforementioned trends. The effect of the haze for various geometries, on the other hand, is not as apparent in the optical performance of CdTe solar cells as the effect of CdS absorption. Haze must be analyzed along with the equivalent CdTe thickness as they both effect the light absorption in CdTe.

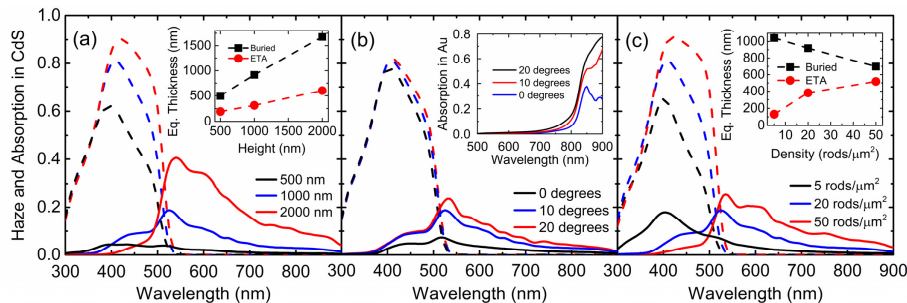


Fig. 3. The absorption spectra of CdS (dashed lines) and haze spectra of ZnO/CdS NRs in the absence of CdTe and Au layers (solid lines) at various (a) NR heights for an angular deviation of 10° and a $20 \text{ rods}/\mu\text{m}^2$ density, (b) angular deviations for a height of 1000 nm and a $20 \text{ rods}/\mu\text{m}^2$ density and (c) NR densities for a height of 1000 nm and an angular deviation of 10° .

Inset of (a): The change of equivalent thickness with the NR height. Inset of (b): The absorption in Au for various angular deviations for an ETA cell with 1000 nm-tall and 50 rods/ μm^2 -dense NRs. Inset of (c): The change of equivalent thickness with the NR density.

Calculation of spatial distribution of photo-generation is required together with the absorption spectrum to analyze the charge collection efficiency of solar cells. Here, we provide the photo-generation analysis only for the buried cells due to their higher MAPC compared to ETA cells'. The photo-generation profiles of the buried cells with a NR density of 20 rods/ μm^2 , an angular deviation of 10° and heights of 500 nm and 2000 nm are given in Figs. 4(a) and 4(b), respectively. The photo-generation is higher near the front surface of the CdTe layer for both geometries due to the high extinction coefficient of CdTe at short wavelengths, leading to a small absorption depth. A solar cell with shorter NRs absorbs light more uniformly compared to a solar cell with longer NRs. The disordered standing wave pattern close to the rear side of the solar cell with 2000 nm-tall NRs is due to interferences at relatively long wavelengths as shown in Figs. 4(b) and 4(c). The photo-generation profile of a solar cell with 50 rod/ μm^2 -dense NRs is similar to that of a solar cell with 20 rods/ μm^2 -dense NRs but the darker red appearance of the disordered standing wave pattern indicates the stronger light trapping by the denser NRs.

The absorption spectra of ITO, ZnO, CdS, CdTe and Au layers for the buried cells having a NR density and height of 20 rods/ μm^2 and 500 nm, 20 rods/ μm^2 and 2000 nm, and 50 rods/ μm^2 and 2000 nm are shown in Figs. 4(d), 4(e), and 4(f), respectively. MAPC and MAPC-equivalent parasitic absorption values for the corresponding NR geometry are given on Figs. 4(d)-4(f), where the MAPC is divided into two regions separated by the band gap of CdS (520 nm), indicated by the dashed lines. The absorption in CdTe and in other layers are nearly the same at wavelengths shorter than 520 nm for the two distinct NR heights since most of the absorption occurs within tens of nanometers in ZnO, CdS and CdTe layers which hinders the effect of the NR height. Besides, the parasitic absorption in ITO is not affected by the NR height, as its thickness is constant. Lastly, there is no parasitic absorption in Au at short wavelengths since light at these wavelengths cannot reach the rear side of the solar cells. At wavelengths longer than 520 nm, the absorption in CdTe dominates since the extinction coefficients of ZnO and CdS are nearly zero. Solar cells with taller NRs produce higher MAPC at longer wavelengths

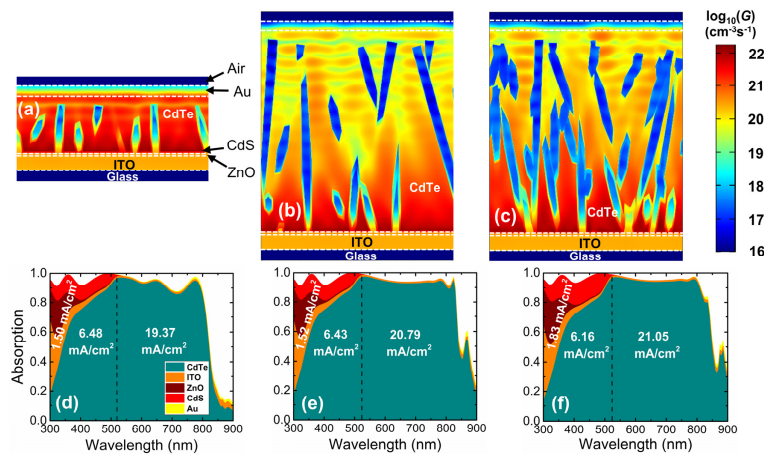


Fig. 4. The photo-generation profiles, (G , in log scale) of buried cells with (a) 500 nm-tall and 20 rods/ μm^2 dense NRs, (b) 2000 nm-tall and 20 rods/ μm^2 -dense NRs and (c) 2000 nm-tall and 50 rods/ μm^2 -dense NRs. The corresponding absorption spectra for cells with (d) 500 nm-tall NRs and 20 rods/ μm^2 density, (e) 2000 nm-tall and 20 rods/ μm^2 -dense NRs and (f) 2000 nm-tall and 50 rods/ μm^2 -dense NRs. Dashed lines indicate to the band gap of CdS. The MAPC equivalent of total parasitic absorption are given on (d), (e) and (f). The MAPC at shorter and

longer wavelengths than the bandgap of CdS are given on the left and right sides of the dashed lines on (d), (e) and (f), respectively.

thanks to the higher haze and equivalent thickness as shown in Figs. 4(d) and 4(e). On the other hand, the MAPC-equivalent total parasitic absorption increases with the NR density as shown Figs. 4(e) and 4(f) as ZnO and CdS volumes also increase with the NR density. However, the enhanced light trapping due to the increased haze at long wavelengths compensates for the parasitic losses in the denser NRs. As a result, the MAPC of solar cells for both NR densities are nearly the same. It is worth noting that the CdS can be replaced with a more transparent window material such as $Mg_xZn_{1-x}O$ to reduce the parasitic absorption [9].

3.2 Electrical simulations

The current density of a solar cell depends on the collection efficiency of photo-generated carriers at the metal contacts. Furthermore, the collection efficiencies of the carriers depend on the electrical conditions (e.g. the defect density, the concentrations of electron and holes with respect to each other) along the path that they travel to reach the respective contacts where they are collected. If a minority carrier or a carrier generated within the space-charge region (SCR) reaches to the quasi-neutral region where it becomes a majority carrier, it can be assumed to be collected. This is because the probability of recombination of a majority carrier traveling to the metal contact is negligible under low-injection conditions, which is satisfied in the configurations analyzed here. On the other hand, if the SCR covers a large portion of the device instead of the quasi-neutral regions, despite the electric field that is in favor of carrier collection within the SCR, the collection efficiency of a particular carrier can be degraded if the recombination rate and the travel length of the carrier to become collected are considerably large. Overall, both the recombination rate within the device and the spatial profile of the SCR are crucial for carrier collection efficiencies and therefore the J_{sc} .

The width of the SCR decreases with the doping concentration (N_A) at the base of a solar cell. Considering a planar CdTe cell with a p -type CdTe base and an n -type CdS layer, a shorter SCR at a higher N_A in CdTe hinders minority electrons to reach the SCR, making the electron collection efficiency the limiting factor. Therefore, taking into account that the majority of the photo-generation occurring within the CdTe base of solar cells, one can expect a reduced J_{sc} with increasing N_A for the planar cells [33]. On the other hand, in the NR-based solar cells, the SCR forms around the physical junction of CdS and CdTe. Therefore, the SCR profile surrounds the ZnO/CdS NRs, including the CdS layer. The profile of the SCR is heavily influenced by the solar cell geometry, and CdTe and CdS doping densities. Besides, the much larger CdS/CdTe area of the NR-based cells compared to that of planar cells makes CdS/CdTe surface vulnerable to the high surface recombination. Hence, the recombination rate at this surface should also be taken into account.

The band bending in the CdTe layer of a buried cell with 500 nm-tall and 20 rods/ μm^2 -dense NRs is illustrated in Fig. 5 under short circuit conditions for N_A of 10^{15} cm^{-3} , 10^{16} cm^{-3} and 10^{17} cm^{-3} . While the red color indicates large band bending and the presence of the SCR, the blue end of the color chart indicates small to no band bending, hence, the lack of the SCR where quasi-neutrality prevails. When N_A is 10^{15} cm^{-3} , as shown in Fig. 5(a), the SCR occupies a large portion of the volume in between the NRs close to the front surface where majority of the light absorption occurs, as shown in the photo-generation profiles in Figs. 4(a)-4(c). The volume of SCR is smaller for an N_A of 10^{16} cm^{-3} (Fig. 5(b)) compared to that of 10^{15} cm^{-3} . For N_A of 10^{17} cm^{-3} (Fig. 5(c)), the SCR is confined to a region closer to the surface of the NRs and occupies a very small portion of the volume in between the NRs. The difference in the volume of the SCR does not significantly affect the distance that minority electrons have to traverse to be collected owing to the lateral collection pathways provided by the surrounding NRs. However, for lowly-doped CdTe layers (i.e. $N_A < 10^{16} \text{ cm}^{-3}$) where the SCR formed around the NRs overlaps, hole collection is significantly more difficult as the

holes have to cross over long distances surrounded by the possibly highly-recombinative CdS/CdTe interface.

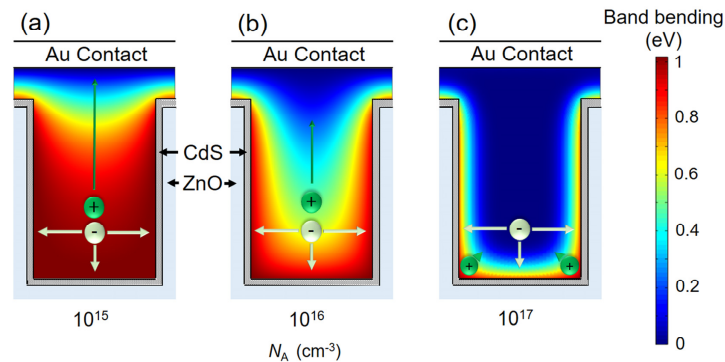


Fig. 5. Band bending in CdTe layer of buried cells with 500 nm-tall and 20 rods/ μm^2 -dense NRs for N_A of (a) 10^{15} , (b) 10^{16} and (c) 10^{17} cm^{-3} . White and green arrows demonstrate the tentative paths of electrons and holes, respectively. White and green circles represent electrons and holes, respectively.

The dependence of J_{sc} on S_F for the buried cells with NR heights and densities of 500 nm and 5 rods/ μm^2 , 500 nm and 20 rods/ μm^2 , and 2000 nm and 5 rods/ μm^2 having N_A of 10^{15} cm^{-3} , 10^{16} cm^{-3} and 10^{17} cm^{-3} is shown in Fig. 6. Additionally, the dependence of J_{sc} on S_F and N_A for planar cells having the same equivalent thickness of the aforementioned buried cells is given for comparison. The results for the buried cells with 50 rods/ μm^2 -dense NRs are not shown since they do not further contribute to the trends discussed in this part.

The rapid loss in J_{sc} with S_F is apparent in the buried cells for all geometries when N_A is 10^{15} cm^{-3} as shown in Fig. 6(a), since the SCR is large and occupies most of the CdTe in between the NRs as demonstrated in Fig. 5(a). In the cells with the shortest and least-dense NRs, a relatively high J_{sc} can be maintained if S_F is kept below 10^4 cm/s . However, for cells with 2000 nm-tall NRs, J_{sc} stays below 10 mA/cm^2 even when S_F is as low as 10 cm/s due to the long path of holes until they reach to the quasi-neutral region. On the contrary to the buried cells, planar cells are much less sensitive to S_F since the hole collection path is short and is not surrounded by defective CdS surfaces. Overall, buried cells with an N_A of 10^{15} cm^{-3} suffer from poor carrier collection due to high surface recombination at the CdS/CdTe interface and are outperformed by their planar counterparts in terms of charge collection efficiency.

The buried cells having an N_A of 10^{16} cm^{-3} with the 5 rods/ μm^2 -dense NRs for all NR heights produce J_{sc} over 25 mA/cm^2 when S_F is lower than 10^4 cm/s as shown in Fig. 6(b) and outperform their planar counterparts, thanks to the shallower SCR (Fig. 5(b)) allowing a higher hole collection efficiency. However, the buried cells with denser NRs are still very vulnerable to surface recombination. As a result, they provide a higher J_{sc} compared to the planar cells only for S_F lower than 10^2 cm/s . Moreover, The SCR is confined to a thin region surrounding the NRs for an N_A of 10^{17} cm^{-3} leading to a high hole collection efficiency, as shown in Fig. 5(c). Hence, J_{sc} is not significantly affected by S_F and the buried cells are advantageous than their planar counterparts for any geometry. The solar cells with 500 nm-tall NRs can produce a J_{sc} of ~ 25 mA/cm^2 and those with 2000 nm-tall NRs can yield a J_{sc} of >27 mA/cm^2 even with S_F as high as 10^5 cm/s .

The volume of the SCR is limited with the CdTe volume in ETA cells for all CdTe doping densities investigated in this study (data not shown). Moreover, unlike the buried cells, the SCR profile does not change significantly with the NR density in ETA cells. As a result, the hole collection efficiency and J_{sc} are not heavily affected by the NR density as shown in Fig. 7(a). Additionally, J_{sc} varies significantly with S_F even at a N_A of 10^{17} cm^{-3} , which was not

the case for the buried cells. The higher J_{sc} of the ETA cell with denser NRs is due to their superior optical performance as shown in Fig. 3.

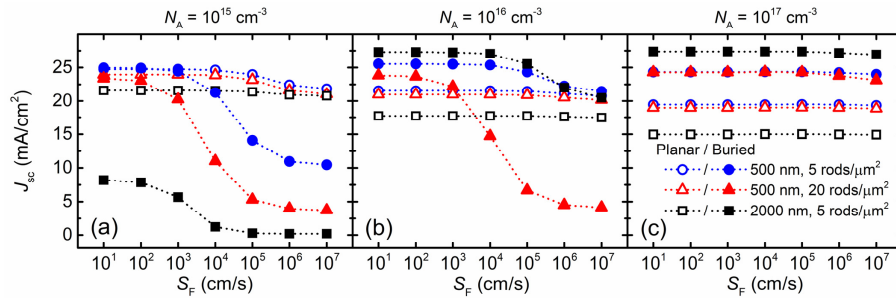


Fig. 6. Effect of surface recombination velocity at the CdS/CdTe interface on the J_{sc} for buried cells with 500 nm-tall and 5 rods/ μm^2 , 500 nm-tall and 20 rods/ μm^2 , and 2000 nm-tall and 5 rods/ μm^2 -dense NRs and planar cells with same equivalent thicknesses for N_A of (a) 10^{15} cm^{-3} , (b) 10^{16} cm^{-3} and (c) 10^{17} cm^{-3} .

J_{sc} of ETA cells having 500 nm and 2000 nm-tall NRs and N_A of 10^{16} cm^{-3} and 10^{17} cm^{-3} with respect to S_F is shown in Fig. 7(b). The charge collection in cells with taller NRs suffers from surface recombination, and as a result, J_{sc} decreases rapidly with S_F especially for small N_A . For example, J_{sc} is lower than 9 mA/ cm^2 for an N_A of 10^{16} cm^{-3} even for a very small S_F of 10 cm/s. J_{sc} values as high as $\sim 17 \text{ mA}/\text{cm}^2$ can be achieved in ETA cells with shorter NRs when S_F is smaller than $10^3 \text{ cm}/\text{s}$. It should be noted that the J_{sc} of ETA cells shown in Fig. 7 further reduces when the recombination velocity at the CdTe/PMMA interface is taken into account (data not shown).

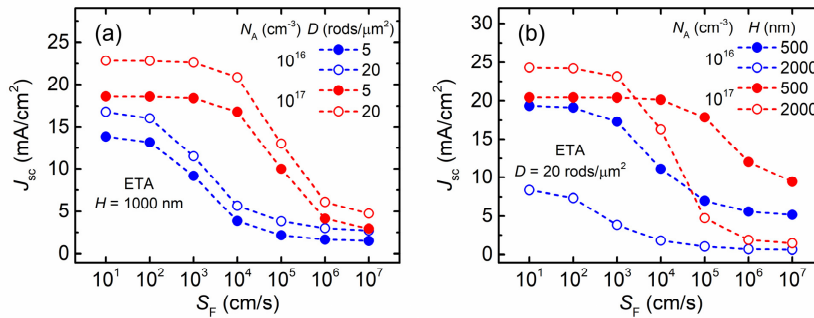


Fig. 7. Effect of CdS/CdTe surface recombination velocity on the J_{sc} for ETA cells with (a) 1000 nm-tall and 5 rods/ μm^2 - and 20 rods/ μm^2 -dense NRs, and (b) 500 nm- and 2000 nm-tall and 20 rods/ μm^2 -dense NRs.

4. Discussion

The equivalent thickness, MAPC, material reduction factor (γ) and J_{sc} of the selected buried and ETA cells are given in Table 1. Material reduction factor is the thickness ratio of a planar cell to the equivalent thickness of a NR-based one when both cells have the same MAPC. Therefore, γ provides an optical performance parameter on materials saving when NR-based cells are used. The J_{sc} of the cells are provided for N_A of 10^{16} cm^{-3} and S_F of $10^4 \text{ cm}/\text{s}$ to ensure applicability using the state-of-the-art materials quality. The highest γ (1.62) in ETA cells can be achieved when NR height and density are equal to 500 nm and 5 rods/ μm^2 , respectively. Additionally, the ETA cells with 500 nm-tall and 20 rods/ μm^2 -dense NRs provide the highest J_{sc} of 11.1 mA/ cm^2 . These values for ETA cells are rather low such that ETA cells cannot provide a distinctive advantage over the planar cells because of their vulnerability to high CdS/CdTe surface recombination, especially for tall NRs, as shown in

Fig. 7(b). Contrarily, γ of buried cells typically increases with the height and density of NRs, and reaches to a maximum of ~ 4 when NR height and density are 2000 nm and 50 rods/ μm^2 , respectively. On the other hand, J_{sc} reduces with NR density for any NR height, and with NR height for dense (20 rods/ μm^2 and 50 rods/ μm^2) NRs due to the enhanced effect of the surface recombination on the hole collection for dense NRs, as shown in Fig. 6(b). Notably, buried cells with NR density of 5 rods/ μm^2 provide a balance between γ and J_{sc} . In particular, γ and J_{sc} of 2.4 and 27.0 mA/cm² can be achieved by the buried cells with a NR height of 2000 nm. In fact, carrier collection efficiency is near unity in this geometry as evidenced by the small difference between the MAPC and J_{sc} . It should be kept in mind that J_{sc} of tall NRs are very sensitive to N_A such that it reduces to 1.2 mA/cm² when the N_A is 10^{15} cm⁻³. Alternatively, a buried cell with 500 nm-tall and 5 rods/ μm^2 -dense NRs can provide moderate γ and J_{sc} of 1.5 and 25.4 mA/cm², respectively; yet, it is less vulnerable to changes in N_A .

Table 1. Equivalent thickness, MAPC, material reduction factors and J_{sc} for selected buried and ETA cell geometries. The J_{sc} values are provided for N_A of 10^{16} cm⁻³ and S_F of 10^4 cm/s. The buried cells have angular deviation of 2θ and the ETA cells have angular deviation of θ .

	NR Height (nm)	NR Density (rods/ μm^2)	Equivalent thickness (nm)	MAPC (mA/cm ²)	Material enhancement factor, γ	J_{sc} (mA/cm ²)
Buried	500	5	560	26.1	1.50	25.4
	500	20	489	25.9	1.45	14.7
	1000	20	891	26.8	1.80	4.9
	2000	5	1992	27.4	2.35	27.0
	2000	50	1298	27.4	3.99	3.1
ETA	500	5	82	19.1	1.62	8.4
	500	20	194	23.3	1.42	11.1
	2000	20	626	24.6	0.65	1.8

Our findings shed light on the previously reported ZnO NR-based CdTe cells, which exhibited J_{sc} values due to utilization of very high ZnO NR densities [6,7,9] or depositing a very thin CdTe layer [5,6,8]. More importantly, in some of the studies utilized ETA type structures [4–6,8] an intentional acceptor doping to the CdTe layer other than the immersion step in CdCl₂ solution has not been performed [4–8,10], hence, the acceptor doping densities were likely to be very low. Here, we limit our electrical analysis to J_{sc} to reveal the potential of NR-based solar cell in terms of light trapping and carrier collection efficiency. The suggestion of higher N_A in NR-based solar cells to achieve higher J_{sc} values can be extended to V_{oc} as it will raise the separation between the Fermi levels of CdS and CdTe.

5. Conclusions

In this study, the light trapping and carrier collection efficiencies of ETA and buried CdTe solar cells are investigated and compared against their planar counterpart. ETA cells' light trapping performance mostly depends on the CdTe amount in the cell, and do not effectively benefit from the light trapping effects of the ZnO NRs. Besides, their hole collection efficiencies are rather low unless very high CdTe doping densities and low CdS/CdTe surface recombination velocities are utilized. Buried cells, on the other hand, benefit from the haze provided by ZnO NRs especially at high angular deviations. Additionally, buried cells allow superior hole collection efficiency than ETA cells and superior electron collection than planar cells at moderate CdTe doping densities (i.e. 10^{16} cm⁻³) and CdS/CdTe surface recombination velocities (i.e. 10^4 cm/s) which are experimentally feasible. Thanks to high light trapping efficiency, the use of CdTe absorber can be significantly reduced when ZnO NRs are incorporated in the form of buried cells without compromising from the high efficiency. Yet, the ZnO NR geometry should be chosen with caution since there is a trade-off between the light trapping and carrier collection efficiencies. As a result, 2000 nm-tall and 5 rods/ μm^2 -dense ZnO NRs provide an optimum geometry when a doping density of 10^{16} cm⁻³ and a

surface recombination velocity of 10^4 cm/s are utilized. Finally, this study provides a guideline to the reader about the sources of low efficiencies reported in the literature for ZnO NR-based CdTe solar cells in terms of ZnO NR geometry and CdTe doping density and CdS/CdTe interface quality to achieve high J_{sc} .

Funding

Scientific and Technical Research Council of Turkey (TUBITAK), (114F518).

Acknowledgments

The authors would like to thank Dr. Giray Kartopu for fruitful discussions.

References

1. S. Shokhovets, O. Ambacher, and G. Gobsch, "Conduction-band dispersion relation and electron effective mass in III-V and II-VI zinc-blende semiconductors," *Phys. Rev. B Condens. Matter Mater. Phys.* **76**(12), 125203 (2007).
2. M. A. Green, Y. Hishikawa, E. D. Dunlop, D. H. Levi, J. Hohl-Ebinger, and A. W. Y. Ho-Baillie, "Solar cell efficiency tables (version 52)," *Prog. Photovolt. Res. Appl.* **26**(7), 427–436 (2018).
3. Fraunhofer ISE: Photovoltaics Report, updated 19 June 2018.
4. V. Consonni, S. Renet, J. Garnier, P. Gergaud, L. Artús, J. Michallon, L. Rapenne, E. Appert, and A. Kaminski-Cachopo, "Improvement of the physical properties of ZnO/CdTe core-shell nanowire arrays by CdCl₂ heat treatment for solar cells," *Nanoscale Res. Lett.* **9**(1), 222 (2014).
5. X. Wang, H. Zhu, Y. Xu, H. Wang, Y. Tao, S. Hark, X. Xiao, and Q. Li, "Aligned ZnO/CdTe core-shell nanowire arrays on indium tin oxide: synthesis and photoelectrochemical properties," *ACS Nano* **4**(6), 3302–3308 (2010).
6. X. Cao, P. Chen, and Y. Guo, "Decoration of textured ZnO nanowires array with CdTe quantum dots: enhanced light-trapping effect and photogenerated charge separation," *J. Phys. Chem. C* **112**(51), 20560–20566 (2008).
7. G. Zhang, S. Jiang, Y. Lin, W. Ren, H. Cai, Y. Wu, Q. Zhang, N. Pan, Y. Luo, and X. Wang, "Improving the photovoltaic performance of solid-state ZnO/CdTe core-shell nanorod array solar cells using a thin CdS interfacial layer," *J. Mater. Chem. A Mater. Energy Sustain.* **2**(16), 5675–5681 (2014).
8. M.-J. Jin, X.-Y. Chen, Z.-M. Gao, T. Ling, and X.-W. Du, "Improve photo-electron conversion efficiency of ZnO/CdS coaxial nanorods by p-type CdTe coating," *Nanotechnology* **23**(48), 485401 (2012).
9. G. Kartopu, D. Turkay, C. Ozcan, W. Hadibrata, P. Aurang, S. Yerci, H. E. Unalan, V. Barrioz, Y. Qu, L. Bowen, A. K. Gürlük, P. Maiello, R. Turan, and S. J. C. Irvine, "Photovoltaic performance of CdS/CdTe junctions on ZnO nanorod arrays," *Sol. Energy Mater. Sol. Cells* **176**(November 2017), 100–108 (2018).
10. J. D. Major, R. Tena-Zaera, E. Azaceta, and K. Durose, "ZnO nanowire radial CdTe solar cells," in *2015 IEEE 42nd Photovoltaic Specialist Conference (PVSC)* (2015), pp. 1–4.
11. R. Tena-Zaera, J. Elias, and C. Lévy-Clément, "ZnO nanowire arrays: Optical scattering and sensitization to solar light," *Appl. Phys. Lett.* **93**(23), 233119 (2008).
12. R.-E. Nowak, M. Vehse, O. Sergeev, K. von Maydell, and C. Agert, "ZnO nanorod arrays as light trapping structures in amorphous silicon thin-film solar cells," *Sol. Energy Mater. Sol. Cells* **125**, 305–309 (2014).
13. J. Jean, S. Chang, P. R. Brown, J. J. Cheng, P. H. Rekemeyer, M. G. Bawendi, S. Grateček, and V. Bulović, "ZnO nanowire arrays for enhanced photocurrent in PbS quantum dot solar cells," *Adv. Mater.* **25**(20), 2790–2796 (2013).
14. J. Michallon, D. Bucci, A. Morand, M. Zanucchi, V. Consonni, and A. Kaminski-Cachopo, "Light absorption processes and optimization of ZnO/CdTe core-shell nanowire arrays for nanostructured solar cells," *Nanotechnology* **26**(7), 075401 (2015).
15. R. Kapadia, Z. Fan, and A. Javey, "Design constraints and guidelines for CdS/CdTe nanopillar based photovoltaics," *Appl. Phys. Lett.* **96**(10), 103116 (2010).
16. T. Ablekim, S. K. Swain, W.-J. Yin, K. Zaunbrecher, J. Burst, T. M. Barnes, D. Kuciauskas, S.-H. Wei, and K. G. Lynn, "Self-compensation in arsenic doping of CdTe," *Sci. Rep.* **7**(1), 4563 (2017).
17. L. Kranz, C. Gretener, J. Perrenoud, R. Schmitt, F. Pianezzi, F. La Mattina, P. Blösch, E. Cheah, A. Chirilă, C. M. Fella, H. Hagedorfer, T. Jäger, S. Nishiwaki, A. R. Uhl, S. Buecheler, and A. N. Tiwari, "Doping of polycrystalline CdTe for high-efficiency solar cells on flexible metal foil," *Nat. Commun.* **4**(1), 2306 (2013).
18. Y. Zhao, M. Boccard, S. Liu, J. Becker, X.-H. Zhao, C. M. Campbell, E. Suarez, M. B. Lassise, Z. Holman, and Y.-H. Zhang, "Monocrystalline CdTe solar cells with open-circuit voltage over 1 V and efficiency of 17%," *Nat. Energy* **1**(6), 16067 (2016).
19. M. C. Akgun, Y. E. Kalay, and H. E. Unalan, "Hydrothermal zinc oxide nanowire growth using zinc acetate dihydrate salt," *J. Mater. Res.* **27**(11), 1445–1451 (2012).
20. A. Belaidi, T. Dittrich, D. Kieven, J. Tornow, K. Schwarzbürg, M. Kunst, N. Allsop, M.-C. Lux-Steiner, and S. Gavrilov, "ZnO-nanorod arrays for solar cells with extremely thin sulfidic absorber," *Sol. Energy Mater. Sol. Cells* **93**(6–7), 1033–1036 (2009).
21. Lumerical Inc, <http://www.lumerical.com/tcad-products/fdtd/>.

22. T. A. F. König, P. A. Ledin, J. Kerszulis, M. A. Mahmoud, M. A. El-Sayed, J. R. Reynolds, and V. V. Tsukruk, "Electrically tunable plasmonic behavior of nanocube-polymer nanomaterials induced by a redox-active electrochromic polymer," *ACS Nano* **8**(6), 6182–6192 (2014).
23. Z. Holman, unpublished data, retrieved from <https://www2.pvlighthouse.com.au> on 17/11/2017.
24. R. E. T. and A. S.-P. and K. D. and K. H. and S. R. and D. Lane, "Optical design and fabrication of fully sputtered CdTe/CdS solar cells," *J. Phys. Conf. Ser.* **286**(1), 12038 (2011).
25. K. M. McPeak, S. V. Jayanti, S. J. P. Kress, S. Meyer, S. Iotti, A. Rossinelli, and D. J. Norris, "Plasmonic films can easily be better: rules and recipes," *ACS Photonics* **2**(3), 326–333 (2015).
26. M. Szczurowski, unpublished data, retrieved from <https://refractiveindex.info> on 17/11/2017.
27. "Atlas User's Manual." www.silvaco.com.
28. M. Burgelman, P. Nollet, and S. Degrave, "Electronic behaviour of thin-film CdTe solar cells," *Appl. Phys., A Mater. Sci. Process.* **69**(2), 149–153 (1999).
29. M. Gloeckler, A. L. Fahrenbruch, and J. R. Sites, "Numerical modeling of CIGS and CdTe solar cells: setting the baseline," in *3rd World Conference on Photovoltaic Energy Conversion, 2003. Proceedings* (2003), **1**(1), p. 491–494.
30. M. Burgelman, P. Nollet, and S. Degrave, "Modelling polycrystalline semiconductor solar cells," *Thin Solid Films* **361–362**, 527–532 (2000).
31. T. Minami, T. Miyata, and T. Yamamoto, "Work function of transparent conducting multicomponent oxide thin films prepared by magnetron sputtering," *Surf. Coat. Tech.* **108–109**, 583–587 (1998).
32. B. Höffling, A. Schleife, F. Fuchs, C. Rödl, and F. Bechstedt, "Band lineup between silicon and transparent conducting oxides," *Appl. Phys. Lett.* **97**(3), 32116 (2010).
33. A. Kanevce and T. A. Gessert, "Optimizing CdTe solar cell performance: impact of variations in minority-carrier lifetime and carrier density profile," *IEEE J. Photovoltaics* **1**(1), 99–103 (2011).